

RHEINISCHE FRIEDRICH-WILHELMS-UNIVERSITÄT BONN

ADVANCED LABORATORY COURSE

PERFORMED ON: APRIL 22, 2022

SUBMITTED ON: MAY 13, 2022

K221: Mößbauer Effect

Authors

Paarth Thakkar
Keito Watanabe

Tutor(s)

Dr. Jens Barth

Abstract

We investigated the hyperfine splitting of the ^{57}Fe using the Mößbauer effect which is the recoilless emission and absorption of photons. A ^{57}Co source was placed with a moving absorber, and the counts corresponding to the 14.4 keV transition of ^{57}Fe was measured. The obtained spectrum yielded more peaks than desired, which were attributed to the Iron (III) oxide from oxidation of the absorber. The linewidth obtained was an order of magnitude larger than the natural linewidth, caused by temperature broadening. The g-factor from the hyperfine spectrum for both excited and ground states were determined, yielding $|g_{\text{exc}}| = 0.0992 \pm 0.0031$ and $|g_{\text{gr}}| = 0.1809 \pm 0.0056$ respectively. The g-factor of the ground state was in excellent agreement with the expected value, while those for the excited state yielded poor agreement, attributing to the asymmetry in the distribution. We obtained the isomer shift as $\delta = (1.026 \pm 0.031) \times 10^{-8}\text{eV}$, which indicates a deviation in excited and ground state monopole energies.

Contents

1	Introduction	2
2	Theoretical Background	3
2.1	Principles	3
2.1.1	Natural Linewidth	3
2.1.2	Recoil and Doppler Shift	4
2.1.3	Debye-Waller Factor	4
2.2	Mößbauer Source	6
2.3	Mößbauer Apparatus and Setup	6
2.4	Isomer Shift	8
2.5	Electric Quadrupole Interaction	9
2.6	Magnetic Dipole Interaction	9
3	Experimental Set-Up	11
4	Calibration	13
5	Mößbauer Spectrum	14
5.1	Spectrum	14
5.2	Natural Linewidth	16
5.3	Hyperfine Splitting	17
5.4	Isomer Shift	18
6	Conclusion and Outlook	19
7	Acknowledgements	20
8	Appendix	22

Chapter 1

Introduction

In this experiment, the phenomenon known as the Mößbauer effect is studied by means of transition spectroscopy. Using a ^{57}Co source, this effect is observed and the hyperfine structure of 14.4 keV transition in ^{57}Fe is measured.

From the Mößbauer spectrum measured, we can see the isomeric shift, quadrupole and magnetic splitting of energy levels. Using this, one can determine the g -factor of the ground state and the first excited state.

In today's report, we will first discuss the theoretical background in Chapter 2. In this section we go through the principles of the Mößbauer effect, which gives us an insight on how the isomer shift, the electric quadrupole interaction and the magnetic dipole interaction give us the observed Mößbauer spectrum. Then in Chapter 3, we look at the experimental set-up used in order to perform the experiment and get the data. In Chapter 4, we look at the decay spectrum of ^{57}Fe , and find the region of interest, which is the Mößbauer line corresponding to 14.4 keV energy difference.

In Chapter 5, we look at the Mößbauer spectrum for absorber moving Left-to-Right (LR) and Right-to-Left (RL), relative to the source for different relative velocities. This allows us to look at the Doppler shift, the isomeric shift and the hyperfine splitting in the energy levels. We also determine the g -factor for the separation of lines between the first excited state and the ground state.

Chapter 2

Theoretical Background

In the following section, we shall study the theoretical background of the Mößbauer effect in brief. A much more detailed discussion can be found in [1], mostly on which the following section is based.

2.1 Principles

Consider two atoms in proximity. If one of the atom's nucleus emits a photon and goes from an excited to a ground state, one might assume that the other nucleus can absorb this photon because the excitation energy of both the nuclei is the same. But that is not the case, since energy is lost by the radiated photon because of the recoil of the nucleus, just like the way a gun recoils when a bullet is fired. In 1957, R. Mößbauer found that this energy reduction in the emitted photon can be reduced if the atom is part of the bigger crystalline structure. In such a situation, the recoil momentum is transferred to the crystal as a whole, which is much more massive than the atom itself and hence the recoil energy is negligible. The recoilless emission and absorption of γ -radiation by the nucleus of an atom is known as the Mößbauer effect [1]. This effect can be seen in Fig. 2.1.1.

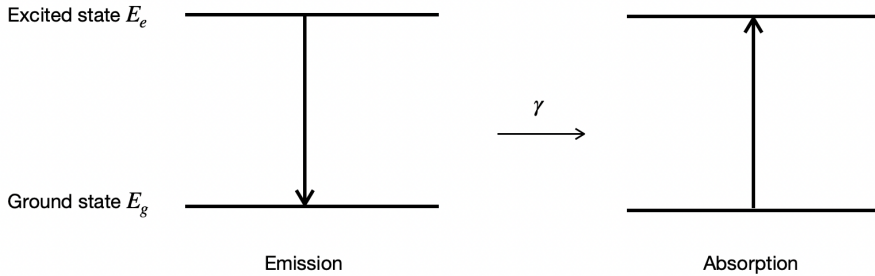


Figure 2.1.1: The recoilless emission and absorption of photon (Mößbauer effect).

2.1.1 Natural Linewidth

The uncertainty in energy in the case of recoilless emission is limited by its natural linewidth. From the Heisenberg's uncertainty principle, we know that

$$\Delta E \Delta t = \hbar, \quad (2.1.1)$$

where ΔE is the energy difference, Δt is the time difference and \hbar is the reduced Planck's constant. In our case, if we have a nuclear level with a mean lifetime of τ_N , the energy uncertainty is given by

$$\Gamma = \hbar / \tau_N. \quad (2.1.2)$$

The frequency spectrum given by this emitted γ -ray is given by a Lorentz distribution,

$$I(\omega) = \frac{I_0}{1 + [2\hbar(\omega - \omega_0)/\Gamma]^2} \quad (2.1.3)$$

where $I(\omega)$ is the intensity of the radiation at frequency ω . The distribution (Fig. 2.1.2) is centered at ω_0 and has a halfwidth of Γ/\hbar . For ^{57}Fe used in this experiment, $\Gamma = 4.7 \times 10^{-9}$ eV.

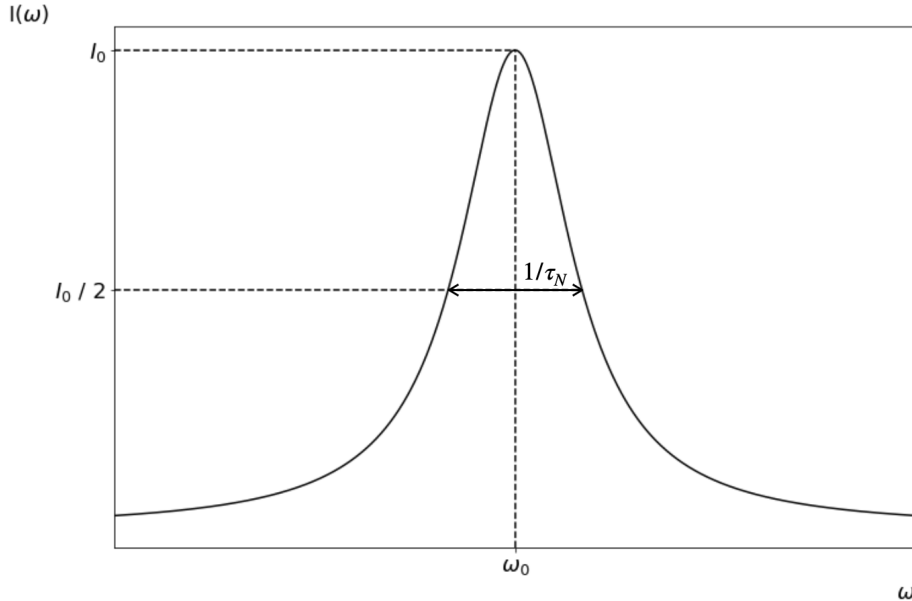


Figure 2.1.2: Intensity distribution of emitted γ -ray, centered at ω_0 with a halfwidth of $1/\tau_N$.

2.1.2 Recoil and Doppler Shift

As discussed in Section 2.1, the recoil of the nucleus when emitting a γ -ray leads to a reduced energy. This can be written as

$$E_{\text{before}} = E_e + \frac{p^2}{2M}, \quad (2.1.4)$$

where, p is the momentum and M is the mass of the nucleus. Energy after the emission can be written as

$$E_{\text{after}} = E_g + \frac{(p - \hbar k)^2}{2M}, \quad (2.1.5)$$

where $\hbar k$ is the momentum of the emitted γ -ray. The energy difference is

$$E_{\text{before}} - E_{\text{after}} \equiv \hbar\omega = \hbar\omega_0 + \hbar(k \cdot v) - \frac{\hbar^2 k^2}{2M}, \quad (2.1.6)$$

where the term $\hbar(k \cdot v)$ is the Doppler effect, which is responsible for shift and broadening of the spectra. At room temperature, the Doppler shift for ^{57}Fe is $\propto 10^{-2}$. The recoil energy $\hbar^2 k^2/2M$ is 2×10^{-3} eV, both of which are orders of magnitude greater than the natural width. The absorption and emission frequency spectrum is shown in Fig. 2.1.3.

2.1.3 Debye-Waller Factor

In a typical tightly bound solid, the energy required to displace an atom from its position is 20 eV. Since the recoil energy of the γ -ray is of the order 10^{-3} eV, there are two possibilities that can occur. One, since the atom cannot be displaced, it is set in a vibrational motion. Or second, if the vibrational motion is not altered by the emission, the recoil energy is absorbed by the entire solid. In a typical solid, the mass of the entire crystal is 10^{20} times more than the mass of the atom and hence the recoil energy is negligible. In this case, we get an unshifted, unbroadened, emission (Mößbauer) line.

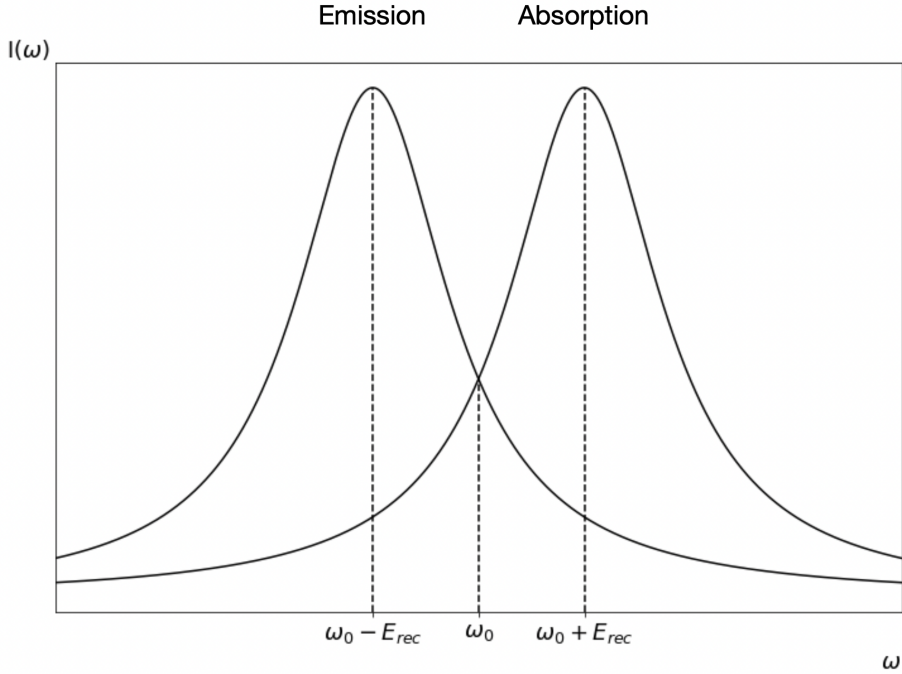


Figure 2.1.3: Emission and absorption spectrum of a monoatomic gas in thermal equilibrium. Both the spectra are shifted by the recoil energy and have been broadened due to Maxwell velocity distribution.

The Debye-Waller factor $f(T)$ is defined is the ratio of the unshifted γ -ray emission to the total number of emissions. This ratio is dependent on temperature and is the highest at $T = 0\text{K}$. But even at absolute zero, $f < 1$ because of zero-point energy.

In order to understand the Mößbauer effect better, one needs to understand the Debye-Waller factor because this factor shows us why the Mößbauer fraction is large. Since the quantum mechanical derivation is a bit too complicated, we look at the semi-classical approach to gain an intuition behind the Debye-Waller factor.

The Semi-classical Approach of the Debye-Waller Factor

Let us consider a nucleus, continuously emitting an electromagnetic wave of frequency $\omega_0 = E_\gamma/\hbar$ and oscillating around an equilibrium point. Considering only one vibration frequency Ω , which corresponds to the Einstein model of the oscillations, the electric field of the emitted radiation is given by

$$E(t) = E_0 \exp(-i[\omega_0 t + kx(t)]), \quad (2.1.7)$$

where $x(t) = a \sin(\Omega t)$, a is the amplitude of the oscillation. Decomposition of this relation in Eqn. 2.1.7 shows that, the effect of vibration of the atom reduces the intensity of the central line by a factor of $(1 - k^2 a^2/4)$ and also produces sidebands with frequencies $\omega_0 \pm \Omega$, $\omega_0 \pm 2\Omega$, and so on.

If we sum up these contributions to the intensity from sidebands to the unshifted line, we get

$$A(\omega_0) = 1 - \frac{k^2 a^2}{4} + \dots = \mathcal{J}_0(ka), \quad (2.1.8)$$

where $\mathcal{J}_0(ka)$ is the Bessel function of zero order. The Debye-Waller factor is given by the absolute square of this quantity.

So far we have considered only a single oscillation mode. When we consider several normal modes (phonons), in which each frequency produces its own sidebands, we need to take the product of all of them (Eqn. 2.1.9).

$$f = \prod_n \mathcal{J}_0^2(ka_n) \approx \prod_n \left(1 - \frac{k^2 a_n^2}{4}\right)^2 \approx \exp(-k^2 \langle x^2 \rangle), \quad (2.1.9)$$

where $\langle x^2 \rangle = \sum a_n^2 / 2$ is the average square displacement. For an isotropic, 3-dimensional oscillator,

$$f = \exp\left(-\frac{k^2 \langle u^2 \rangle}{3}\right), \quad (2.1.10)$$

where $\langle u^2 \rangle = 3 \langle x^2 \rangle$, the average square displacement. In quantum mechanics, this $\langle u^2 \rangle$ becomes the expectation value.

Going back to the Einstein model, where only single vibration frequency Ω is considered, we can derive the temperature dependence for the Debye-Waller factor. Taking the harmonic energy with n excited quanta, we calculate the occupation probability and obtain the Bose-Einstein distribution function. Using this result, we then generalize for a phonon distribution function $Z(\Omega)$ and calculate the dependence for 3-dimensions. The result we obtain is

$$f(T) = \exp\left(-\frac{\hbar k^2}{6MN} \int_0^\infty \frac{Z(\Omega)}{\Omega} \left[1 + \frac{2}{\exp(\hbar\Omega/k_bT) - 1}\right] d\Omega\right), \quad (2.1.11)$$

where N is the number of molecules in the solid.

The following important conclusions can be deduced:

1. By measuring the Debye-Waller factor, one can obtain the phonon frequency spectrum.
2. The Debye-Waller factor decreases with increase in the recoil energy.
3. Large Mößbauer effect can be observed at low temperatures, which is because of the fact that the Debye-Waller factor is maximum at absolute zero. Hence, low temperatures are favorable for measurement.

2.2 Mößbauer Source

There are several requirements for a Mößbauer source. These are:

1. The γ -ray transition must go to the ground state, since for a stable isotope, absorption can only take place from the ground state.
2. The Debye-Waller factor must not be too small. In order to achieve that, we must have low temperatures, low γ -ray energy, high Debye temperature and high atomic mass.
3. The lifetime should not be too short, otherwise due to Eqn. 2.1.2, we will have a poor energy resolution.
4. The source should be practical (easy to obtain, handle and so on).

There are several possible sources for studying the Mößbauer effect, many of these are discussed in detail in [1]. In this experiment, we used isotope ^{57}Co as the source. The decay scheme is shown in Fig. 2.2.1.

The Mößbauer source $^{57}\text{Co}-^{57}\text{Fe}$ is an ideal choice because the parent isotope, ^{57}Co has long half-life (270 days), which enables one to perform several experiments with the same source. The lifetime of the Mößbauer level is sufficiently long, giving us a good energy resolution. Lastly, the energy level of 14.4 keV is small enough to allow for the conduction of experiment at room temperature.

2.3 Mößbauer Apparatus and Setup

A schematic representation of the setup is shown in Fig. 2.3.1. Here, we have a radioactive source, an absorber and a detector. In the diagram, the source is moving with respect to the absorber but in our setup, the source was stationary and the absorber was moving. However, this does not affect the measurement, since the relative motion is constant.

There are two possible arrangements in the setup: transmission geometry and scattering geometry. In transmission geometry, we record the intensity of γ -rays transmitted. While in scattering geometry, the fluorescence radiation is measured. In order to achieve the resonance condition (similar to what can be seen in Fig. 2.3.1), we move the absorber relative to the source (or vice versa). A loudspeaker principle

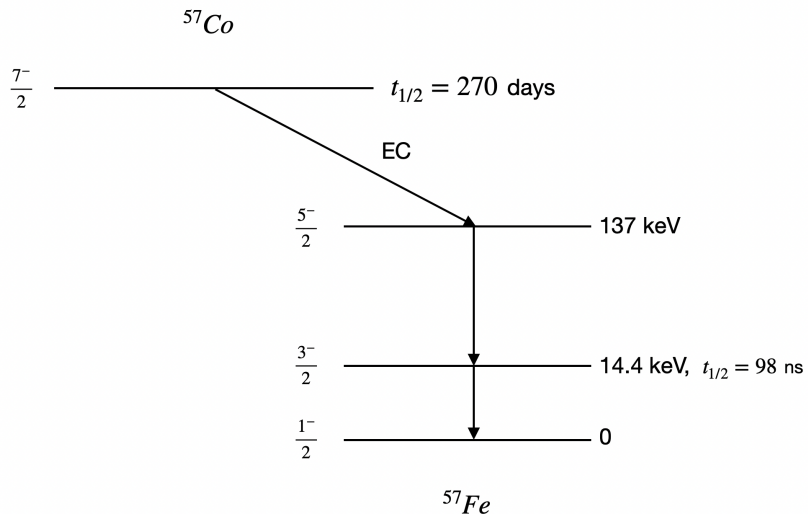


Figure 2.2.1: Decay scheme of ^{57}Co . The decay occurs largely (99.8%) due to Electron Capture (EC). The nuclear moments of Mößbauer level ($I = 3/2$) and ground level ($I = 1/2$) are shown here.

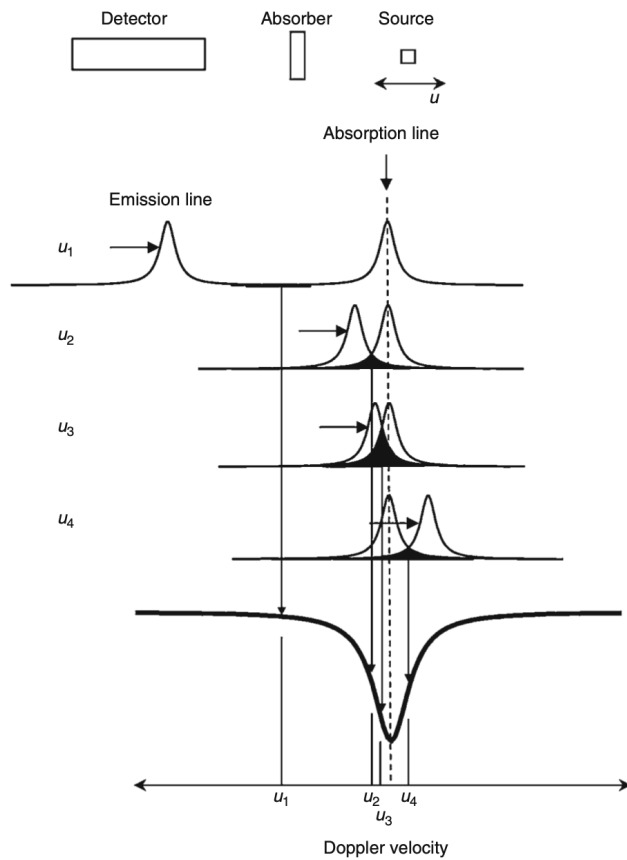


Figure 2.3.1: A representation of the setup of the experiment. In our case, the absorber moves while the source remains stationary. The Doppler principle is seen by the scanning of the absorption line with the emission line. The resultant intensity is proportional to the addition of absorption and emission lines, which are marked at four arbitrary chosen velocities between u_1 and u_4 [2].

is often used to produce these oscillations. On these oscillations, velocity profiles can be imposed by using driver coils, using a function generator.

The γ -ray detector is often made of scintillators or gas-filled proportional counters. These detect the intensity of γ -rays that pass through the absorber. The pulse height that we get with a proportional counter with 97% Kr and 3% CO₂, is shown in Fig. 2.3.2. The line corresponding to 14.4 keV is the Mößbauer line. This is the region that we study in the experiment in order to get the Mößbauer spectrum.

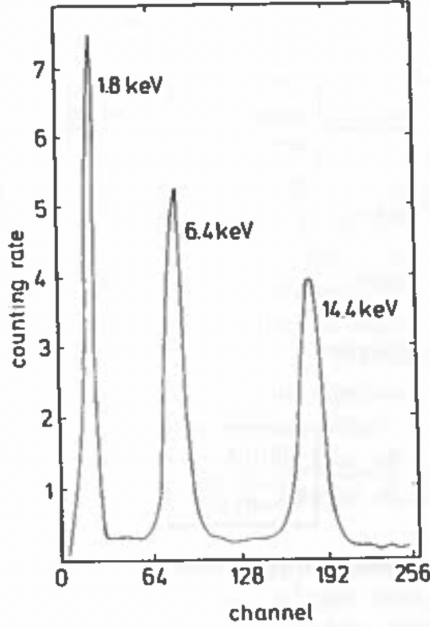


Figure 2.3.2: Pulse height spectrum measured using gas-filled proportional counter. The 14.4 keV Mößbauer line is shown. [1].

2.4 Isomer Shift

A shift in the resonance of the spectrum occurs in the Mößbauer experiment due to difference in the monopole energy in the ground state and excited state. The monopole energy is given by

$$E_c = \frac{Ze^2}{6\epsilon_0} |\Psi(0)|^2 \langle r^2 \rangle, \quad (2.4.1)$$

where $\langle r^2 \rangle$ is the mean square radius of the nuclei.

For a moving absorber, the energy difference between excited (e) to ground state (g) is given by

$$\hbar\omega(A) = \hbar\omega_0 \left(1 + \frac{v}{c}\right) + \frac{Ze^2}{6\epsilon_0} |\Psi_A(0)|^2 (\langle r_e^2 \rangle - \langle r_g^2 \rangle), \quad (2.4.2)$$

where the first term corresponds to Doppler shift due to the motion of the absorber. For a stationary absorber,

$$\hbar\omega(S) = \hbar\omega_0 + \frac{Ze^2}{6\epsilon_0} |\Psi_S(0)|^2 (\langle r_e^2 \rangle - \langle r_g^2 \rangle). \quad (2.4.3)$$

For the resonance condition to be fulfilled, $\omega(S) = \omega(A)$, the velocity of the absorber must be

$$v_{res} = \frac{Ze^2 c}{6\epsilon_0 \hbar\omega_0} \left(|\Psi_A(0)|^2 - |\Psi_S(0)|^2 \right) (\langle r_e^2 \rangle - \langle r_g^2 \rangle), \quad (2.4.4)$$

where v_{res} is the isomer shift. By convention, this value is positive when the absorber is moving towards the source. For ⁵⁷Fe, this value is negative since the radius of the nuclei in the excited state is smaller than the of ground state. Typically, the order of isomer shift is of the order of several mm s⁻¹.

2.5 Electric Quadrupole Interaction

Electric quadrupole interaction occurs in the presence of electric field gradient, which leads to non-spherical nucleus when the nuclear spin $I \geq 1$. In this case the degeneracy of the m sub-levels is lifted and we get a splitting of energy levels. As can be seen in Fig. 2.5.1, the energy level splitting does not depend on the sign of m , for instance, $m = \pm 3/2$ are indistinguishable.

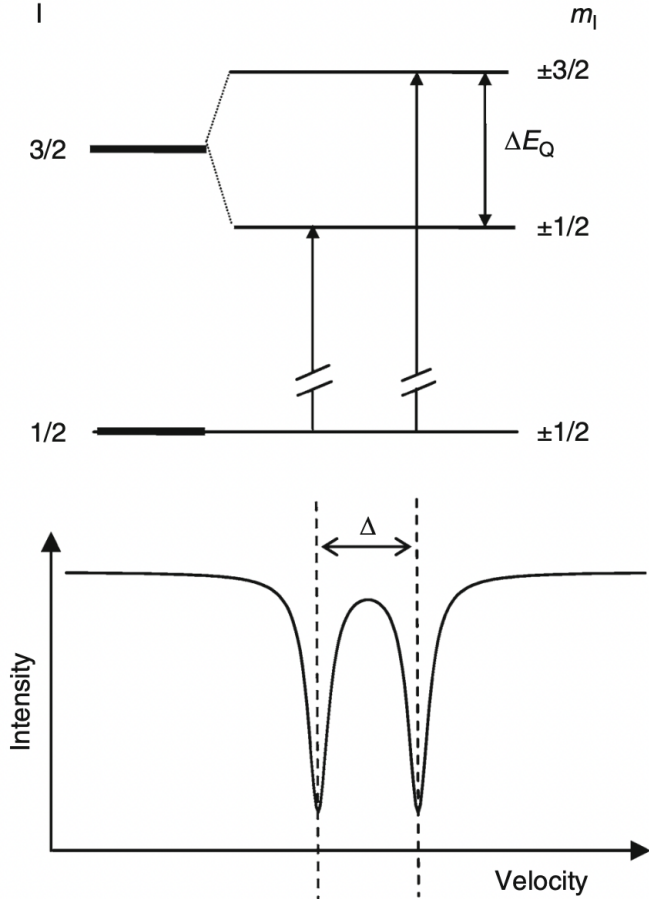


Figure 2.5.1: Quadrupole splitting of $I = 3/2$ and the corresponding Mößbauer spectrum [2].

The energy separation that can be seen Fig. 2.5.1, is given by

$$\Delta E = 6\hbar\omega_Q = \hbar\omega_0 \frac{\Delta v}{c}, \quad (2.5.1)$$

where Δv is the separation in between two lines in velocity spectrum given by

$$\Delta v = \frac{eQV_{zz}c}{2\hbar\omega_0}. \quad (2.5.2)$$

In the case of powder sample of ^{57}Fe , we get equal amplitude of Mößbauer lines. This is because the electric field gradient are distributed statistically, which leads to the γ -rays being emitted isotropically.

2.6 Magnetic Dipole Interaction

Magnetic dipole interaction leads to further splitting in the energy levels of the sub-levels. This is a result of magnetic interaction ($-\vec{\mu} \cdot \vec{B}$) splitting the magnetic sub-levels equally, consequently splitting the energy levels of the emitted γ radiation. Fig. 2.6.1 shows the magnetic splitting for ^{57}Fe .

Experimentally, only six lines are transitions are observed and therefore we can conclude that this follows the M1 selection rules, according to which $|m| \leq 1$. The transition energies are given by

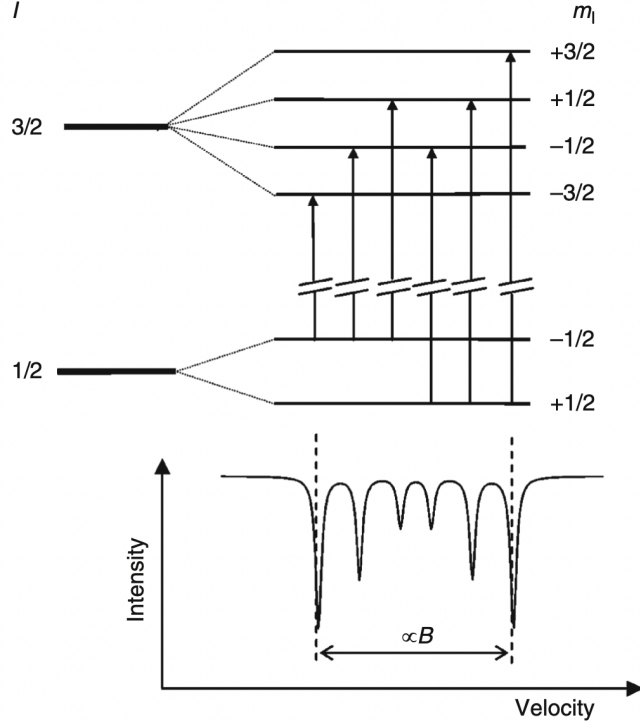


Figure 2.6.1: The magnetic splitting of energy levels and the corresponding Mößbauer spectrum of ^{57}Fe [2].

$$\hbar\omega(m_e \rightarrow m_g) = \left(E_e - \frac{\mu_e}{I_e} m_e B \right) - \left(E_g - \frac{\mu_g}{I_g} m_g B \right) \quad (2.6.1)$$

$$= \hbar\omega_0 - \left(\frac{\mu_e}{I_e} m_e - \frac{\mu_g}{I_g} m_g \right) B. \quad (2.6.2)$$

The resonant velocity is given by

$$v_{res} = -\frac{c}{\hbar\omega_0} \left(\frac{\mu_e}{I_e} m_e - \frac{\mu_g}{I_g} m_g \right) B. \quad (2.6.3)$$

The magnetic hyperfine structure can be given by the Hamiltonian

$$H = -\mu \cdot B = -g\mu_N I B, \quad (2.6.4)$$

where μ is the magnetic moment and μ_N is the nuclear magneton [2]. Since the magnetic energy is given by $E_m = g\mu_N M B$, the energy perturbation due to hyperfine splitting is given by

$$E_m = -g\mu_N B. \quad (2.6.5)$$

Chapter 3

Experimental Set-Up

To measure the Mößbauer spectrum, we placed a ^{57}Co radioactive source onto a table with a moving absorber that has a maximum displacement of 25.1 ± 0.2 mm. A photodetector is placed behind the absorber that detects the number of photons that are not absorbed via this process. The speed of the absorber is controlled by a motor that swings the absorber at a fixed velocity. See Fig. 3.0.1 for the Mößbauer source apparatus. In our experiment, we vary the absorber velocity up until 7.5 mm/s.

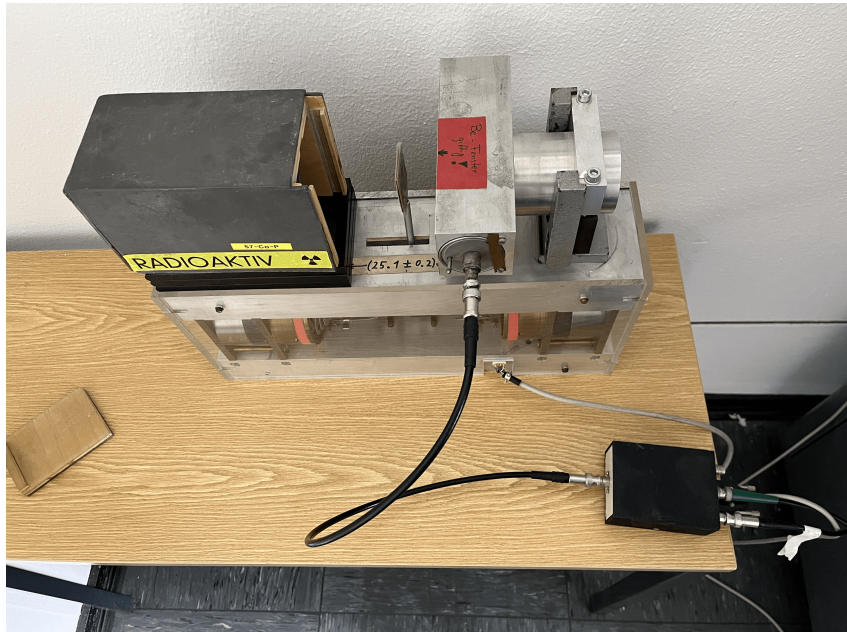


Figure 3.0.1: The set-up of the Mößbauer source. *Left:* The ^{57}Co source. *Middle:* The moving absorber. *Right:* The photodetector which is connected to the detector apparatus.

The photodetector is then connected to a single channel analyzer (SCA), which displays the number of counts N detected in a given time range T . The SCA has 2 main parameters that should be modified: the Upper Level Discriminator (ULD) and the Lower Level Discriminator (LLD). The ULD and LLD controls the range in which we detect the counts, and the ULD can further control the bin-size of the measurement. The modes of the ULD can be set to measure with a higher resolution by detecting counts with 10 % of the bin-size. The SCA was then connected to a display in which the number of counts obtained in a specific time interval was shown.

The photo-detecting apparatus consists of two SCA that allows measurements for absorber velocities in both positive (RL) and negative (LR) directions. This is required since the offset voltage between the two directions can allow the measurements to differ. This gives us counts $N(\text{RL} / \text{LR})$ and time intervals $T(\text{RL} / \text{LR})$ for each direction. A separate run counter that tracks the number of turns made by the absorber is also contained in the apparatus. We also use a separate timer that controls the time interval of measurement for the calibration process. The set-up is constructed in a way such that the count and time measurements terminate only after the absorber had performed a full turn. See Fig. 3.0.2 for the

apparatus used for the photo-detection as well as the schematic of the apparatus.

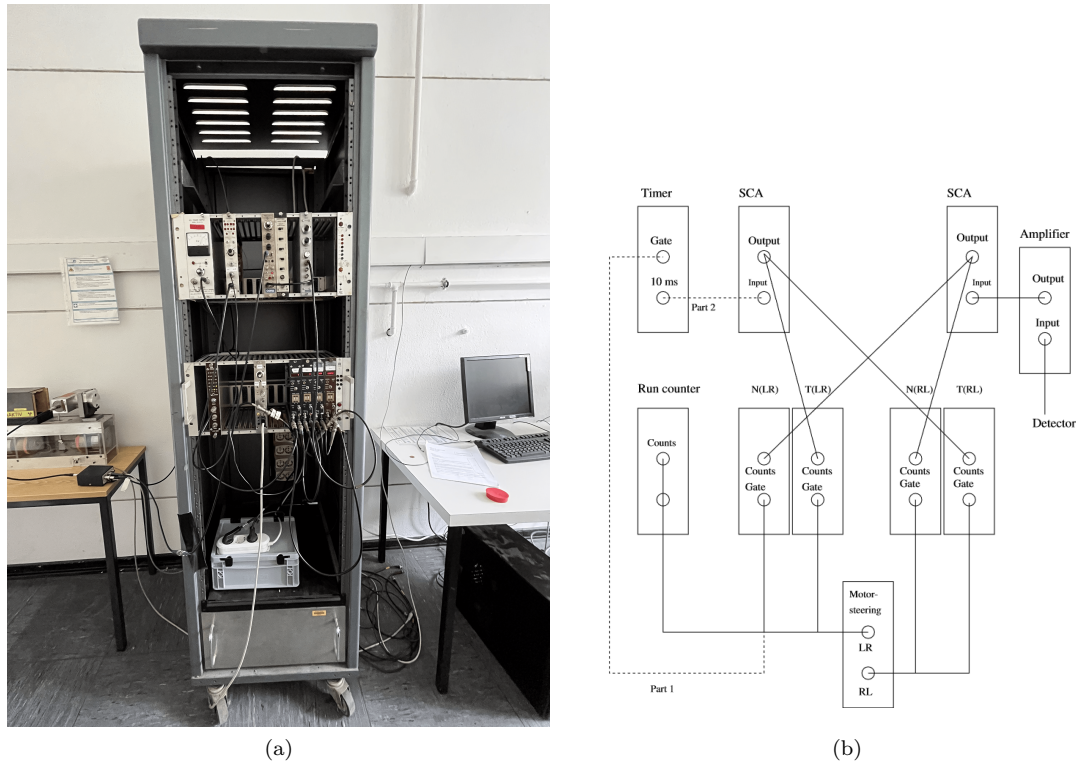


Figure 3.0.2: (a) The photodetector apparatus used in this experiment. (b) The schematic of the apparatus. Obtained from Ref. [3].

Chapter 4

Calibration

Before we took any measurements, we determined the optimal values for the LLD in order to ensure that we are detecting counts from the 14.4 keV transition. In order to do so, we modified the LLD from 0 to 4 and determined the number of counts obtained at each value for a fixed time interval for $T = 10$ s. Once the data was obtained, we plotted the number of detected photons N against the LLD values and compared our results to the ^{57}Fe γ -spectrum as seen in Fig. 2.3.2. This allowed us to identify the range in which we should set the ULD and LLD values when performing the Mößbauer measurements. Fig. 4.0.1 shows the obtained spectrum from our experiment. See the Appendix section (Chapter 8) for the full data obtained from this section. The uncertainty for the counts were taken to be purely statistical such that $\delta N = \sqrt{N}$, and the uncertainty of the time interval measurement was taken to be $\delta T = \pm 0.003$ s.

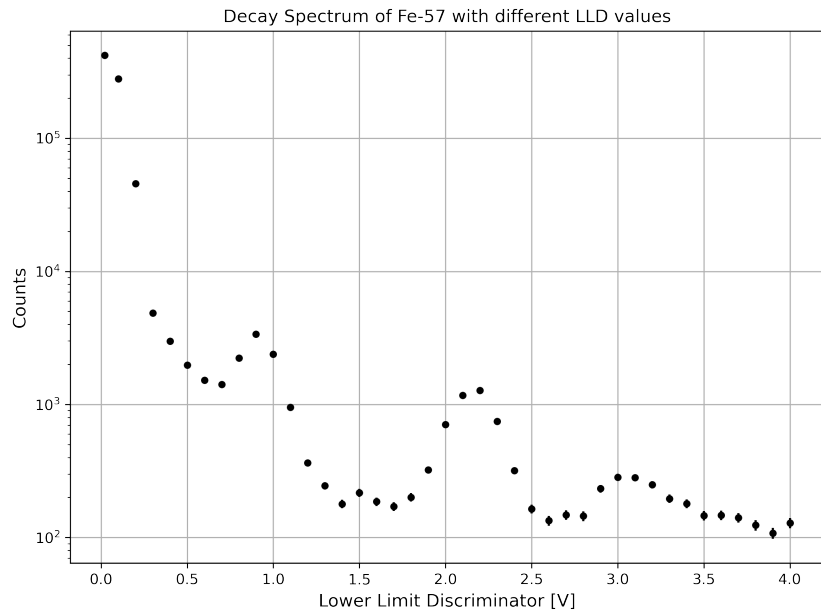


Figure 4.0.1: The pulse height spectrum for ^{57}Fe decay observed in the experiment. The number of counts are shown for varying LLD values.

By comparison to expected results, we identified the 14.4 keV transition line as the third peak on Fig. 4.0.1. The ULD and LLD values that were used to perform the Mößbauer measurement was then set to be 1.8V and 2.6V respectively.

Chapter 5

Mößbauer Spectrum

5.1 Spectrum

To observe the Mößbauer spectrum, we first set the ULD and LLD to 1.8V and 2.6V respectively as obtained from Chapter 4. Once a certain motor speed has been set, we ran both LR and RL single channel analyzers for a set number of turns, ranging from 4 to 10 turns. We then recorded the obtained number of counts and duration for both LR and RL analyzers. This was repeated until we obtained enough points to more accurately construct the Mößbauer peaks. This was verified by using the built-in plotting tool in Excel where we displayed the plot between the count rate $R = N/T$ against the motor speed. We took a total of 60 measurements in this experiment, ranging for motor speeds from 0V to 2.5V. Fig. 5.1.1 shows the raw data obtained from both analyzers. See Appendix (Chapter 8) for the raw data table obtained from both analyzers.

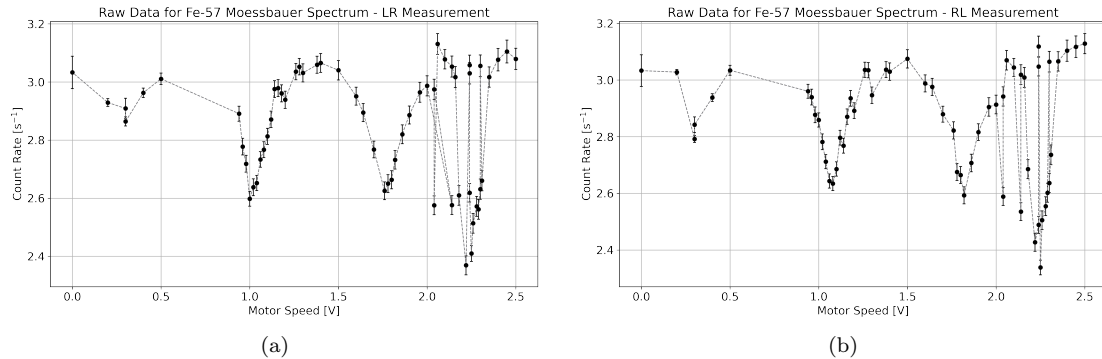


Figure 5.1.1: The Raw Spectrum obtained from the Mößbauer measurement for the 14.4 keV transition for ^{57}Fe from the (a) LR and (b) RL single channel analyzer. Several outliers can be observed.

The uncertainty of the count rate was calculated using the standard Gaussian error propagation formula using δN , δT as in Chapter 4:

$$\delta R = R \sqrt{\left(\frac{\delta N}{N}\right)^2 + \left(\frac{\delta T}{T}\right)^2} = R \sqrt{\left(\frac{\sqrt{N}}{N}\right)^2 + \left(\frac{\delta T}{T}\right)^2}. \quad (5.1.1)$$

To determine the peaks, we first filtered out the outliers from the data, then combined the LR and RL measurements to construct the full Mößbauer spectrum. Fig. 5.1.2 shows the combined Mößbauer measurement after filtering.

We then performed a non-linear fit to the multi-Lorentz distribution, i.e. the sum of Lorentz distributions, to determine the peak velocity v_0 , peak amplitude I_0 , and the full-width half-maximum of the peaks (FWHM) Γ_v for each observed peak. The offset δ_I from a full symmetric distribution was also determined through this fitting process. The equation used to fit is shown as such:

$$I_{tot}(v, v_{0i}, I_{0i}, \Gamma_{vi}, \delta_I) = \delta_I + \sum_{i=1}^{N_{\text{peaks}}} -I_{0i} \frac{(\Gamma_{vi}/2)^2}{(v - v_{0i})^2 + (\Gamma_{vi}/2)^2}. \quad (5.1.2)$$

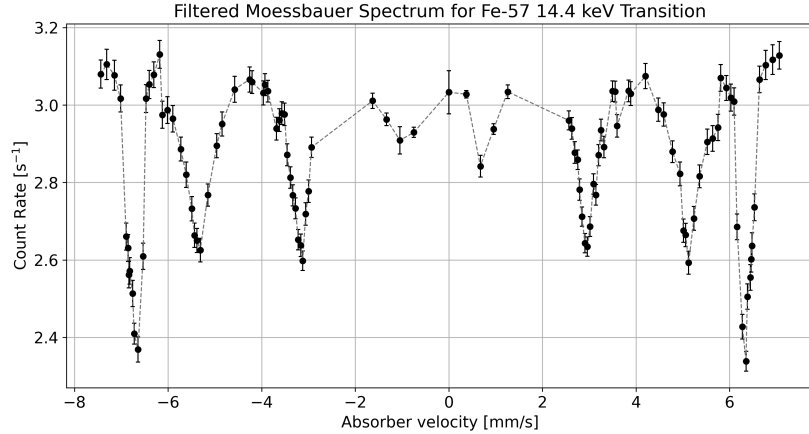


Figure 5.1.2: The Mößbauer spectrum after removing outliers and combining the LR and RL data.

The fitting procedure was implemented using the Python package `lmfit` which utilizes the Levenberg-Marquardt method.

Fig. 5.1.3 shows the full Mößbauer spectrum with the obtained multi-Lorentzian fit, and Table 5.1 shows the obtained fit parameters from the analysis for each peak. The offset was determined to be $\delta_I = 3.162 \pm 0.025 \text{ s}^{-1}$. We also show the spectrum against the individual Lorentzian peaks that composed our total fit in Fig. 5.1.4. The uncertainties were obtained from the covariance matrix evaluated through the fitting procedure. In the Appendix section (Chapter 8) we show the fit using the initial guess parameters.

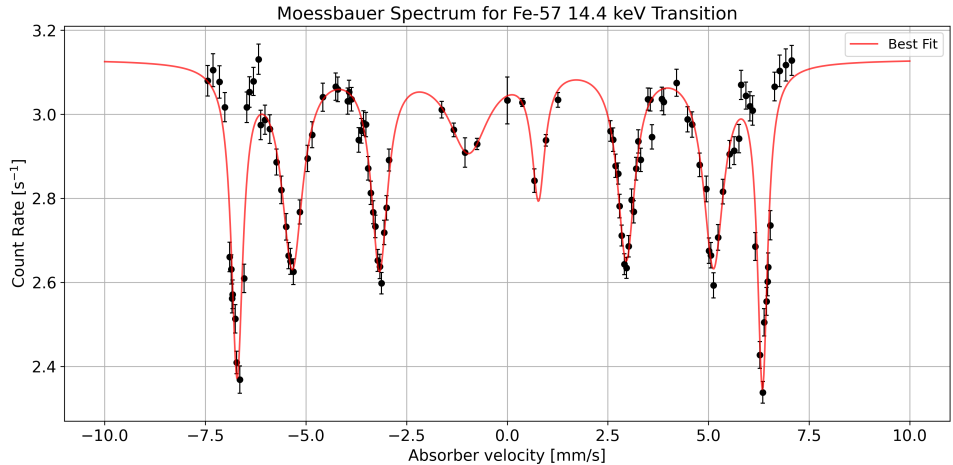


Figure 5.1.3: The observed Mößbauer spectrum for ^{57}Fe through the 14.4 keV transition for varying absorber velocities. The non-linear Lorentzian fit is also shown.

From Fig. 5.1.3, we observe a total of eight peaks, contrary to the six peaks that are expected from the hyperfine splitting of the ^{57}Fe spectrum. After calculating for the isomer shift and g-factors in the following sections, we observed that the first and last peaks were outliers that may have not have been a result of the 14.4 keV transition of ^{57}Fe . A possible explanation of the additional peaks is due to the oxidation of the absorber. As the instrument may be relatively old, the iron may have oxidized, creating impurities within the absorber. The oxidation of the iron will have caused some of the iron to form into iron (III) oxide which consists of Fe_2O_3 , FeO , and Fe_3O_4 . When performing Mößbauer spectroscopy onto such molecules, one observes finer splitting at absorber velocities of around $6 - 8 \text{ mm s}^{-1}$, which is what we also observe from Fig. 5.1.3 [4]. As of such, we removed the first and last peaks for the following sections.

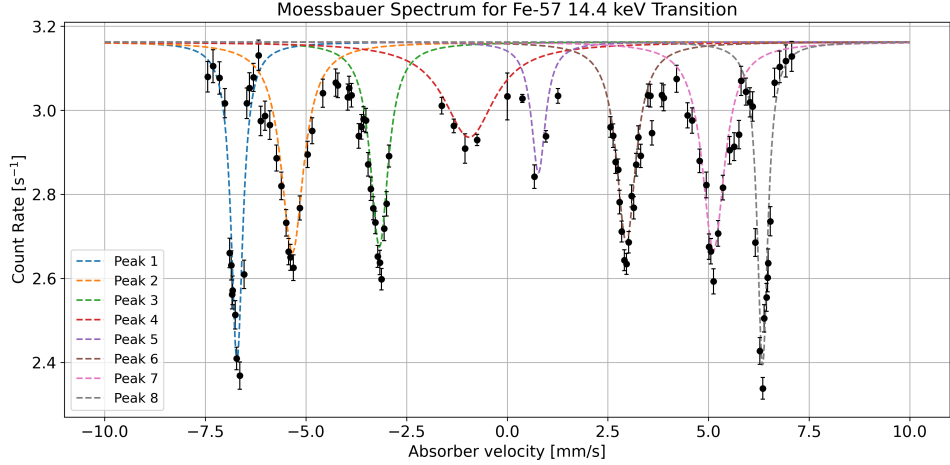


Figure 5.1.4: Same as Fig. 5.1.3 but showing the individual components of the fit instead.

Peak	v_0 [mm s $^{-1}$]	I_0 [s $^{-1}$]	Γ_v [mm s $^{-1}$]	$\delta_I - I_0$ [s $^{-1}$]
1	-6.7131 ± 0.0097	0.759 ± 0.039	0.352 ± 0.033	2.403 ± 0.046
2	-5.335 ± 0.026	0.501 ± 0.036	0.682 ± 0.096	2.661 ± 0.043
3	-3.174 ± 0.016	0.487 ± 0.030	0.538 ± 0.066	2.674 ± 0.039
4	-0.94 ± 0.14	0.226 ± 0.034	1.54 ± 0.77	2.935 ± 0.042
5	0.776 ± 0.033	0.311 ± 0.080	0.43 ± 0.20	2.851 ± 0.084
6	2.958 ± 0.015	0.476 ± 0.028	0.583 ± 0.064	2.685 ± 0.038
7	5.124 ± 0.025	0.496 ± 0.034	0.673 ± 0.094	2.666 ± 0.042
8	6.3449 ± 0.0089	0.770 ± 0.038	0.315 ± 0.029	2.392 ± 0.045

Table 5.1: Fit parameters v_0 , I_0 , and Γ_v obtained for each peak. The peak values $\delta_v - I_0$ as shown in Fig. 5.1.3 is also presented. The peak is numbered from the left most peak to the rightmost peak.

5.2 Natural Linewidth

To compare the obtained peaks to the analytical results from the hyperfine splitting of the ^{57}Fe nucleus through the 14.4 keV transition, we convert the fit parameters described in the absorber velocity into the transition energy E_γ using the equation describing the Doppler shift of the ground state energy:

$$E = E_0 \left(1 + \frac{v}{c}\right) \implies E_\gamma = \Delta E = E_0 \frac{v}{c}, \quad (5.2.1)$$

where E_0 is the expected ground state energy $E_0 = 14.4$ keV. The FWHM were converted in a similar fashion. Table 5.2 shows the energy value ΔE and its FWHM Γ for each observed peak.

Peak	E_γ [1×10^{-7} eV]	Γ [1×10^{-9} eV]
2	-2.561 ± 0.012	16.3 ± 2.3
3	-1.5238 ± 0.0079	12.9 ± 1.5
4	-0.453 ± 0.069	36 ± 18
5	0.372 ± 0.015	10.2 ± 4.9
6	1.4201 ± 0.0073	14.0 ± 1.5
7	2.460 ± 0.012	16.1 ± 2.2

Table 5.2: The energy values at the peaks E_γ and the FWHM, Γ , obtained for each peak. The peaks are labelled as given in Table 5.1, where the outliers are omitted.

We then evaluated the average linewidth and its corresponding error using the weighted mean as such:

$$\Gamma_{\text{avg}} = \frac{1}{2} \frac{\sum_{i=1}^{N_{\text{peaks}}} \Gamma_i \delta \Gamma_i^{-2}}{\sum_{i=1}^{N_{\text{peaks}}} \delta \Gamma_i^{-2}}, \quad \delta \Gamma_{\text{avg}} = \frac{1}{2} \sqrt{\left(\sum_{i=1}^{N_{\text{peaks}}} \delta \Gamma_i^{-2} \right)^{-1}}, \quad (5.2.2)$$

where the $1/2$ is incorporated as the linewidth is defined as half of the FWHM of the peak.

Using Eqn. 5.2.2, we obtained an average linewidth of $\Gamma_{\text{avg}} = (1.428 \pm 0.090) \times 10^{-8} \text{ eV}$. Comparing this to the natural linewidth of the 14.4 keV transition of $\Gamma_0 = 4.7 \times 10^{-9} \text{ eV}$, we observe that the linewidths we obtained are an order of magnitude larger. A possible cause for this may be due to the Doppler broadening that is caused by the temperature in the room in which the experiment was conducted in. This is due to the fact that at high temperature the vibrations of the atoms within both the source and the absorber yield larger uncertainties in the transition energies of the ^{57}Fe nucleus. In the future, this experiment should be conducted in a colder environment to reduce such broadening.

5.3 Hyperfine Splitting

Fig. 5.1.3 show the multiple peaks that correspond to the hyperfine splitting through electric quadrupole and magnetic dipole transitions of the ^{57}Fe nucleus. As the spectrum splits both at the excited state and at the ground state, we evaluated the g-factor for both the excited and ground state which we denote as g_{exc} and g_{gr} respectively.

We use Eqn. 2.6.5 to determine the g-factor using the magnetic field of the nucleus of $H = 33.3 \pm 1.0 \text{ T}$ as given in Ref. [3] and the nuclear magneton as $\mu_N = 3.152 \times 10^{-8} \text{ eV T}^{-1}$:

$$g = \frac{\Delta E}{\mu_N H}. \quad (5.3.1)$$

In order to use this equation, we first determined the energy values between the peaks. For the excited states, we compare between the peaks that induce the same transition, i.e. the difference of energy values between each peak. The peak-to-peak difference between the two middle peaks (peaks 4 and 5) were omitted as they do not represent transitions through excited states. Table 5.3 shows the energy values between such peaks.

Peaks	$\Delta E_{\text{exc}} [1 \times 10^{-7} \text{ eV}]$
2 - 3	1.037 ± 0.015
3 - 4	1.070 ± 0.069
5 - 6	1.047 ± 0.017
6 - 7	1.039 ± 0.014

Table 5.3: Peak-to-peak energy values, corresponding to energies for hyperfine splitting in the excited state. The peaks are defined as with before.

From this, we obtain a weighted average excited transition energy of $\Delta E_{\text{exc,avg}} = (1.0413 \pm 0.0089) \times 10^{-7} \text{ eV}$ using the weighted average formula similarly to Eqn. 5.2.2. Using Eqn. 5.3.1, we obtain a g-factor for the excited state as $|g_{\text{exc}}| = 0.0992 \pm 0.0031$. This yields values that are 2.19σ values away from to the expected value of the g-factor of the excited state $|g_{\text{exc,thr}}| = 0.106$ [5]. This indicates that our obtained values are in not in good agreement with the expected value.

To find the corresponding g-factor of the ground state, we first determine the energy values between peaks from the $+v$ and $-v$ directions, which yields the total transition energy due to the splitting of both excited and ground states. The energy difference due to the hyperfine splitting of the ground state is then obtained by subtracting the contribution from the average excited state energy obtained above, i.e.

$$\Delta E_{\text{gr}} = \Delta E_{\text{exc+gr}} - \Delta E_{\text{exc}}. \quad (5.3.2)$$

Table 5.4 shows the ground state transition energies for each peak.

Peaks	$\Delta E_{\text{exc+gr}} [1 \times 10^{-7} \text{ eV}]$	$\Delta E_{\text{gr}} [1 \times 10^{-7} \text{ eV}]$
2 - 5	2.934 ± 0.020	1.885 ± 0.028
3 - 6	2.944 ± 0.011	1.895 ± 0.022
4 - 7	2.913 ± 0.071	1.864 ± 0.073

Table 5.4: Same as Table 5.3 but for the ground state. The total excitation energy is also shown.

From Table 5.4, we obtained the weighted average ground state splitting energy $\Delta E_{\text{gr,avg}} = (1.899 \pm 0.012) \times 10^{-7} \text{ eV}$, which gives us a g-factor of $|g_{\text{gr}}| = 0.1809 \pm 0.0056$. Comparing with the expected value

of $|g_{\text{gr,thr}}| = 0.181$, we observe that our results is 0.18σ values away, which indicates excellent agreement [5].

We observe that while we obtain excellent agreement with the ground state g-factor, we do not obtain good results for the excited state g-factor. A possible cause of this may be due to the asymmetry in the distribution. We observe that Peak 4 has much larger broadening compared to other peaks, which may cause deviation in the peak energy. In the future, more data-points should be taken in regions where peak values are located to obtain an even better resolution for the measurement.

5.4 Isomer Shift

We measure the isomer shift by taking the energy difference between the pair of similar peaks obtained from the $+v$ and $-v$ directions, i.e. the furthermost peaks, the middle peaks, and the two innermost peaks. As the spectrum is ideally symmetric, by observing the deviation from the two peaks we observe the deviation of the difference from the zero value. This will yield the desired isomer shift. Table 5.5 shows the resulting values for each pair of peaks.

Peaks	ΔE_{pair} [1×10^{-7} eV]
2 - 7	0.1012 ± 0.0059
3 - 6	0.1037 ± 0.0036
4 - 5	0.080 ± 0.024

Table 5.5: The energy difference between each similar pair of peaks, which is used to determine the isomer shift.

We then obtained the isomer shift by taking the weighted average of the energy difference values. From this, we yielded $\delta = (1.026 \pm 0.031) \times 10^{-8}$ eV, indicating a clear difference in the energies of the ground and excited state of the electric monopole.

Chapter 6

Conclusion and Outlook

In this paper we investigated the hyperfine structure of the ^{57}Fe decay at the 14.4 keV transition energy utilizing the Mößbauer effect. The Mößbauer effect is the recoilless emission and absorption of photons. This effect is observed by moving the source or the absorber relative to each other. This allows measurements up to the order of 1×10^{-9} eV and thus can observe phenomena which requires precision such as the isomer shift and hyperfine splitting of nuclei.

In our experiment, a ^{57}Co source was placed near a moving ^{57}Fe absorber, and the transmission of photons through the absorber was measured using a single channel analyzer. The setup was first calibrated so that only counts resulting from the 14.4 keV Mößbauer transitions are obtained when performing the measurement. This was performed by varying the channel parameter to obtain the γ -spectrum of ^{57}Fe and identifying the peak that corresponds to the 14.4 keV transition.

The absorber was then set to various velocities and the corresponding counts were measured. After removing outliers from the measurement, we obtained the desired Mößbauer spectrum for ^{57}Fe . Two additional peaks were observed, but we considered them as outliers that possibly originate from the iron oxide that is formed due to oxidation of the iron.

The corresponding spectrum was then fitted using a sum of Lorentzian functions, and from this we obtained the amplitudes, peak energies, and FWHM of each peak. From this we obtained a linewidth of $\Gamma_{\text{avg}} = (1.428 \pm 0.090) \times 10^{-8}$ eV, which is an order of magnitude larger than the natural linewidth. This is expected due to Doppler broadening due to temperature fluctuations.

To determine the g-factor of the excited and ground state, we obtained the peak-to-peak energy. For the excited state, the energy difference between each peak was taken, and with the given magnetic field we obtained our g-factor to be $|g_{\text{exc}}| = 0.0992 \pm 0.0031$, which is 2.7σ away from the expected value. For the ground state, the excited state energy was subtracted from the energy difference between every third peak, yielding a g-factor of $|g_{\text{gr}}| = 0.1809 \pm 0.0056$. The results obtained for the ground state were 0.18σ away, indicating excellent agreement. This deviation was attributed to the asymmetry between the left and right side of the distribution.

To determine the isomer shift, the energy difference between pairs of peaks were taken, yielding $\delta = (1.026 \pm 0.031) \times 10^{-8}$ eV. The large isomer shift indicates that there are large deviations between the monopole energy of the ground and excited state.

In the future, we can obtain finer measurements for the spectrum, which would yield in a more precise spectrum. Further, multiple measurements should be taken for each point, which will reduce the statistical uncertainty. This project can be extended by observing the temperature dependence of the Debye-Waller factor or comparing the spectrum between different Mößbauer sources.

Chapter 7

Acknowledgements

We would like to take this moment and thank Dr. Barth, who was really helpful and patient with us throughout the whole experiment. We appreciate him guiding us through the experiment, especially at times at which we were confused. Next, we would like to thank Advanced Lab Course Module for giving us an opportunity to study hyperfine structure of ^{57}Fe with such a simple setup. It is especially interesting to us that with such a setup, we were able to observe phenomena which otherwise requires a much more advanced setup.

Bibliography

- [1] G. Schatz, G. Schatz, A. Weidinger, and J. Gardner, *Nuclear Condensed Matter Physics: Nuclear Methods and Applications*. Wiley, 1996, ISBN: 9780471954798. [Online]. Available: <https://books.google.de/books?id=xMDvAAAAMAAJ>.
- [2] E. Kuzmann, Z. Homonay, S. Nagy, and K. Nomura, “Mössbauer spectroscopy,” in *Handbook of Nuclear Chemistry*, A. Vértes, S. Nagy, Z. Klencsár, R. G. Lovas, and F. Rösch, Eds. Boston, MA: Springer US, 2011, pp. 1379–1446, ISBN: 978-1-4419-0720-2. DOI: [10.1007/978-1-4419-0720-2_25](https://doi.org/10.1007/978-1-4419-0720-2_25). [Online]. Available: https://doi.org/10.1007/978-1-4419-0720-2_25.
- [3] P106: Advanced Laboratory Course, *K221 Mößbauer Effect*, Jul. 2016.
- [4] J. Winsett, A. Moilanen, K. Paudel, *et al.*, “Quantitative determination of magnetite and maghemite in iron oxide nanoparticles using mössbauer spectroscopy,” *SN Applied Sciences*, vol. 1, no. 12, p. 1636, Nov. 2019, ISSN: 2523-3971. DOI: [10.1007/s42452-019-1699-2](https://doi.org/10.1007/s42452-019-1699-2). [Online]. Available: <https://doi.org/10.1007/s42452-019-1699-2>.
- [5] A. F. Vanin and E. van Faassen, “Chapter 5 - low-molecular dinitrosyl iron complexes can catalyze the degradation of active centers of iron–sulfur proteins,” in *Radicals for Life*, E. Van Faassen and A. Fyodorovich Vanin, Eds., Amsterdam: Elsevier, 2007, pp. 119–137, ISBN: 978-0-444-52236-8. DOI: <https://doi.org/10.1016/B978-044452236-8/50005-8>. [Online]. Available: <https://www.sciencedirect.com/science/article/pii/B9780444522368500058>.

Chapter 8

Appendix

In the following section, we include all the data which was measured while performing the experiment and an additional plot.

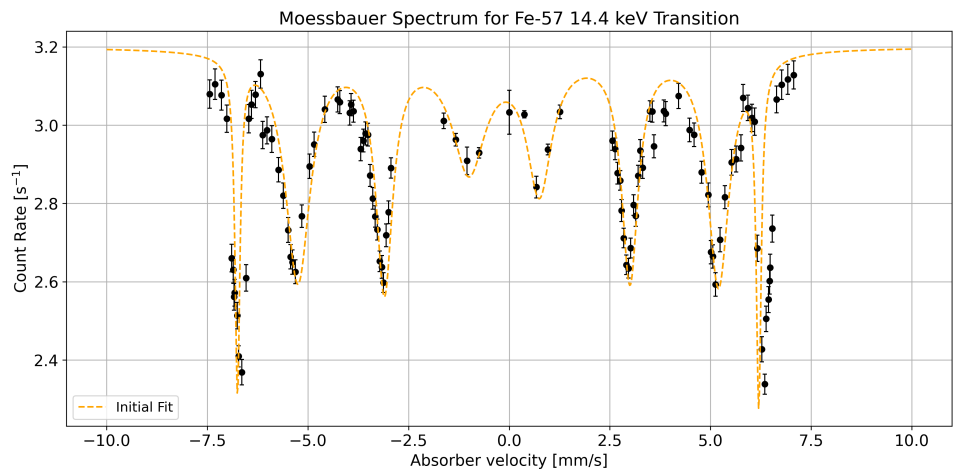


Figure 8.0.1: The Mößbauer spectrum with the fit using the initial guess parameters.

LLD (V) \pm 0.01	Count (N)	Time (s) \pm 0.003	ULD (ΔE) (100%) (10^{-1}) (V)
0.02	420580	10	10
0.10	279704	10	10
0.20	45643	10	10
0.30	4853	10	10
0.4	2982	10	10
0.5	1981	10	10
0.6	1522	10	10
0.7	1412	10	10
0.8	2227	10	10
0.9	3368	10	10
1	2386	10	10
1.1	952	10	10
1.2	365	10	10
1.3	245	10	10
1.4	179	10	10
1.5	217	10	10
1.6	186	10	10
1.7	171	10	10
1.8	201	10	10
1.9	322	10	10
2	705	10	10
2.1	1169	10	10
2.2	1275	10	10
2.3	745	10	10
2.4	319	10	10
2.5	164	10	10
2.6	134	10	10
2.7	148	10	10
2.8	145	10	10
2.9	233	10	10
3	284	10	10
3.1	282	10	10
3.2	249	10	10
3.3	196	10	10
3.4	180	10	10
3.5	146	10	10
3.6	147	10	10
3.7	141	10	10
3.8	124	10	10
3.9	108	10	10
4	129	10	10

Table 8.1: Calibration of the single channel analyzer. Where, Lower Limit Discriminator (LLD) and Upper Level Discriminator (ULD).

Velocity (mm/s)	Motor speed (V)	Count (N)	Time (ms)	Turns	Count/s (N/s)
0	0	3030	999	0	3.03303303303303
0.375400077772128	0.2	101223	33431	5	3.02781849181897
0.674368619022031	0.3	10578	3722	1	2.8420204191295
0.959174574867843	0.4	46130	15701	6	2.9380294248774
1.25827150591538	0.5	30264	9974	5	3.03428915179467
2.56488861639076	0.94	14484	4893	5	2.96014714898835
2.62964903090623	0.96	11223	3818	4	2.93949711891042
2.68952585052237	0.98	10741	3733	4	2.87731047414948
2.7564243356029	1	13016	4553	5	2.85877443443883
2.79276773296245	1.02	10000	3595	4	2.78164116828929
2.84580498866213	1.04	11958	4410	5	2.71156462585034
2.90913305516922	1.06	11403	4314	5	2.6432545201669
2.96340023612751	1.08	11156	4235	5	2.63423848878394
3.01827801827802	1.1	11168	4158	5	2.68590668590669
3.09037182959862	1.12	11355	4061	5	2.79610933267668
3.14142678347935	1.14	11058	3995	5	2.76795994993742
3.19989801121877	1.16	11258	3922	5	2.87047424783274
3.25551232166018	1.18	11316	3855	5	2.93540856031128
3.31659619450317	1.2	10942	3784	5	2.89164904862579
3.49663338750871	1.26	13076	4307	6	3.03598792663107
3.55608028335301	1.28	12852	4235	6	3.03471074380165
3.59701920321009	1.3	10279	3489	5	2.94611636572084
3.84085692425402	1.38	11906	3921	6	3.03647028819179
3.89026658400496	1.4	9773	3226	5	3.02944823310601
4.20576407506702	1.5	9175	2984	5	3.07473190348525
4.47814451382694	1.6	10048	3363	6	2.98780850431163
4.59146341463415	1.64	9760	3280	6	2.97560975609756
4.78225367446924	1.7	10579	3674	7	2.87942297223734
4.94418910045962	1.76	8596	3046	6	2.8220617202889
5.0133155792277	1.78	8037	3004	6	2.6754327563249
5.06218487394958	1.8	7927	2975	6	2.66453781512605
5.12593601089176	1.82	7618	2938	6	2.5929203539823
5.24008350730689	1.86	7780	2874	6	2.70702853166319
5.35997559487492	1.9	9231	3278	7	2.81604636973764
5.52660550458716	1.96	7916	2725	6	2.90495412844037
5.64044943820225	2	7779	2670	6	2.91348314606742
5.7546809323653	2.04	7699	2617	6	2.94191822697746
5.81018518518519	2.06	7957	2592	6	3.06983024691358
5.93180283592167	2.1	9017	2962	7	3.04422687373396
6.03123748498198	2.14	7538	2497	6	3.01882258710453
6.09716599190283	2.16	7432	2470	6	3.00890688259109
6.1620294599018	2.18	6563	2444	6	2.68535188216039
6.275	2.22	5826	2400	6	2.4275
6.32241813602015	2.24	6916	2779	7	2.48866498740554
6.35264341957255	2.25	8315	3556	9	2.33830146231721
6.38135593220339	2.26	5912	2360	6	2.50508474576271
6.44415917843389	2.28	5970	2337	6	2.55455712451861
6.46629454701589	2.29	6060	2329	6	2.60197509660799
6.4802065404475	2.3	6127	2324	6	2.63640275387263
6.53362255965293	2.31	6306	2305	6	2.73579175704989
6.64272211720227	2.35	8109	2645	7	3.06578449905482
6.77158273381295	2.4	6902	2224	6	3.10341726618705
6.92413793103448	2.45	6780	2175	6	3.11724137931034
7.06757843925986	2.5	7777	2486	7	3.1283185840708

Table 8.2: Velocity measurements for Right to Left (RL).

Velocity (mm/s)	Motor speed (V)	Count (N)	Time (ms)	Turns	Count/s (N/s)
-7.44176196526895	2.5	7271	2361	7	3.07962727657772
-7.31067961165049	2.45	6396	2060	6	3.10485436893204
-7.14760322733745	2.4	6483	2107	6	3.07688656858092
-7.0167731629393	2.35	7554	2504	7	3.0167731629393
-6.8956043956044	2.31	5810	2184	6	2.66025641025641
-6.854802002731	2.3	5780	2197	6	2.63086026399636
-6.83923705722071	2.29	5641	2202	6	2.56176203451408
-6.82065217391304	2.28	5678	2208	6	2.57155797101449
-6.75942549371634	2.26	5600	2228	6	2.51346499102334
-6.72521583804704	2.25	8093	3359	9	2.40934802024412
-6.64314071460079	2.22	5370	2267	6	2.36876929863255
-6.53362255965293	2.18	6015	2305	6	2.60954446854664
-6.47185217017619	2.16	7020	2327	6	3.01675977653631
-6.40033999150021	2.14	7184	2353	6	3.0531236719082
-6.30426982418371	2.1	8579	2787	7	3.07822030857553
-6.1771944216571	2.06	7633	2438	6	3.13084495488105
-6.12444082960553	2.04	7315	2459	6	2.97478649857666
-6.01437699680511	2	7479	2504	6	2.98682108626198
-5.89663273296789	1.96	7572	2554	6	2.96476115896633
-5.73059360730594	1.9	8849	3066	7	2.88617090671885
-5.61311964219158	1.86	7566	2683	6	2.81997763697354
-5.49434512951478	1.82	7489	2741	6	2.73221452024808
-5.43486106098881	1.8	7381	2771	6	2.66365932876218
-5.38241601143674	1.78	7415	2798	6	2.65010721944246
-5.31216931216931	1.76	7443	2835	6	2.62539682539683
-5.15098211668133	1.7	9440	3411	7	2.76751685722662
-4.96210873146623	1.64	8786	3035	6	2.89489291598023
-4.8486799742434	1.6	9166	3106	6	2.95106245975531
-4.57862094126231	1.5	8334	2741	5	3.04049616928128
-4.25856803529013	1.4	9035	2947	5	3.06582965727859
-4.20670391061453	1.38	10952	3580	6	3.05921787709497
-3.9652448657188	1.3	9594	3165	5	3.03127962085308
-3.92801251956182	1.28	11704	3834	6	3.05268648930621
-3.86748844375963	1.26	11822	3894	6	3.03595274781715
-3.68683901292597	1.2	10004	3404	5	2.93889541715629
-3.6229792147806	1.18	10256	3464	5	2.96073903002309
-3.57041251778094	1.16	10471	3515	5	2.97894736842105
-3.51147174034695	1.14	10635	3574	5	2.97565752658086
-3.45825296224855	1.12	10420	3629	5	2.87131441168366
-3.38731443994602	1.1	10422	3705	5	2.81295546558704
-3.33244822092406	1.08	10420	3766	5	2.76686139139671
-3.27847439916405	1.06	10463	3828	5	2.73328108672936
-3.21794871794872	1.04	10344	3900	5	2.65230769230769
-3.16320100819156	1.02	8372	3174	4	2.63768115942029
-3.12266733018164	1	10441	4019	5	2.59790992784275
-3.05817849527871	0.98	8925	3283	4	2.71855010660981
-2.99880525686977	0.96	9299	3348	4	2.77747909199522
-2.93429974281038	0.94	12364	4277	5	2.89081131634323
-1.62902388369678	0.5	23197	7704	5	3.01103322949117
-1.33003620948512	0.4	33549	11323	6	2.96290735670759
-1.04496253122398	0.3	6987	2402	1	2.90882597835137
-0.746668253212756	0.2	49236	16808	5	2.92931937172775
0	0	3030	999	0	3.03303303303303

Table 8.3: Velocity measurements for Left to Right (LR).